A Wide-Range Global Optimal Control Strategy for Wireless Charging Systems in Electric Vehicles

Haoze Li, *Graduate Student Member, IEEE*, Linlin Tan, *Member, IEEE*, Heqi Xu, *Student Member, IEEE*, Zhijun Wu, *Graduate Student Member, IEEE*, and Xueliang Huang, *Member, IEEE*

***Abstract*—Maintaining the high efficiency of the wireless charging system for electric vehicles in the full power range is the key point and difficulty in the application. In this article, a wide-range global optimal control (WGOC) method based on the battery impedance characteristics is proposed. Compared with the existing control methods, the losses of the circuits at all levels in the wide operating range are comprehensively considered to achieve the optimization of battery charging over a wide power range. The charging demand of the battery is responded to by the current closed-loop on the secondary side, and the overall efficiency of the system is dynamically optimized by the primary side. The active rectifier implements zero voltage switching and synchronous rectification for the entire cycle. An efficiency model based on the battery load is developed to obtain the optimal curve. The steady-state parameters and the efficiency for a wide power range are accurately calculated. Finally, a 3.5 kW prototype is developed. The experimental results verify the accuracy of the parametric model. Moreover, the WGOC improves the efficiency in all power ranges and the efficiency improvement is up to 9.5% for light load. The applicability of the WGOC is also verified.**

***Index Terms*—Active rectifier, efficiency model, global optimal control, wireless power transfer, zero-voltage switching.**

I. Introduction

WIRELESS charging technology for electric vehicles is currently a research hotspot in the field of electric vehicle charging [1], [2]. Flexible adjustment of charging power and high charging efficiency are important factors that need to be considered in current technology promotion. During the charging process of electric vehicles, as the charging power changes, the load characteristics of the battery change accordingly [3], [4]. For wireless charging systems that are sensitive to impedance characteristics, this means that it is difficult to maintain high charging efficiency at a consistent level [5], [6]. Therefore, how to adapt to changes in battery load characteristics in real time and maintain high efficiency across the full power range during the electric vehicle charging process is a key and challenging issue in the application.

The conventional primary side control (PSC) method adjusts power by changing the input voltage or phase-shift angle of the primary side inverter, with the secondary side being an uncontrolled diode rectifier. Since there is only one control object, the PSC method cannot simultaneously improve efficiency while controlling power [7]. To address this issue, two types of methods have been proposed. One is to add a dc–dc converter on the secondary side for impedance matching to optimize efficiency [8], [9], [10]. In [11], the output voltage is controlled by a dc–dc converter at the load side and the voltage ratio between the primary and secondary side is regulated by a front-side converter to maximize the efficiency. However, this approach introduces additional device losses and severe losses in the diode rectifier at high power levels. An alternative approach is to utilize an active rectifier in place of a diode rectifier on the secondary side [12], [13], [14]. This method introduces a control object into the secondary side circuit, which facilitates efficiency optimization and avoids the necessity for additional devices [15], [16]. In recent years, scholars have conducted research into several control methods for wireless power transfer (WPT) systems with dual active bridges.

In [17], load matching is performed by a semiactive rectifier on the secondary side, and constant power output is achieved by frequency modulation on the primary side. The power loop of this control strategy requires wireless communication. In [18], the regulation of equivalent impedance is realized based on an active rectifier, but the output voltage is controlled by the primary side and the voltage feedback requires wireless communication. In [19], a control method aiming at minimizing zero voltage switching (ZVS) current and minimizing reactive current is proposed based on the LCC-S compensation system. However, the efficiency under light load is significantly degraded. In [20], a secondary-side control strategy to achieve minimum reactive power and ZVS is proposed based on a T-compensation network. However, the primary side control is not considered, and the optimized power range is limited. In [21], a three-phase-shift control is proposed for the double-sided LCC system, and the phase-shift angle for realizing load matching and ZVS is derived, but the operation control loop is not given. In [22] and [23], control strategies for realizing ZVS during constant-current and constant-voltage charging are proposed. However, the global

Manuscript received 6 May 2024; revised 25 June 2024; accepted 28 July 2024. Date of publication 2 August 2024; date of current version 7 October 2024. This work was supported in part by the Qing Lan Project of Jiangsu, in part by the National Natural Science Foundation of China under Grant 52277004, and in part by the Project of Jiangsu Provincial Key Laboratory of Smart Grid Technology and Equipment, Southeast University. Recommended for publication by Associate Editor Y. Tang. *(Corresponding author: Linlin Tan.)*

The authors are with the School of Electrical Engineering, Southeast University, Nanjing 210096, China (e-mail: 230218321@seu.edu.cn; tanlinlin@seu.edu.cn; 230208773@seu.edu.cn; 230218882@seu.edu.cn; xlhuang@seu.edu.cn).

Color versions of one or more figures in this article are available at https://doi.org/10.1109/TPEL.2024.3437180.

Digital Object Identifier 10.1109/TPEL.2024.3437180

efficiency of the system is not analyzed based on the charging load characteristics of the battery.

In general, the majority of current studies aim to achieve ZVS or reactive current minimum for optimization purposes. However, there are numerous sources of losses in WPT systems, particularly in high-order topologies such as double-sided LCC compensation. The losses of double-sided LCC compensated systems mainly include coils losses, compensation inductors losses, and the conduction and switching losses of power switches [21]. When the operating state is changed, the trend of the losses is different at each point. For example, at constant power, as the inverter output voltage decreases, the current through the primary side compensation inductor increases, but the current through the transmitter coil decreases. This indicates the necessity for a global efficiency optimization strategy to achieve optimal overall efficiency. The realization of ZVS or the minimization of reactive current at the output of the inverter does not necessarily result in optimal global efficiency. Furthermore, studies that optimize and control based on battery load characteristics are less frequently observed.

In order to address the aforementioned research gaps and to consider the power control and efficiency optimization of the wireless charging system for electric vehicles with a wide power range, a global optimal control method based on the battery impedance characteristics is proposed for the dual active bridge topology. To prioritize the stability and fast response of the output control, a current closed loop is constructed on the secondary side. The optimization of the global efficiency is implemented by the primary side controller. The double-sided LCC compensated WPT system is chosen in this article due to the advantages of constant coil current on the primary side and bidirectional transmission [24].

The rest of this article is organized as follows. In Section II, the driving methods of the active bridges on the primary and secondary sides are presented, the ZVS and synchronous rectification of the active rectifier are implemented, and then the dual-sided control loop is proposed. In Section III, the impedance characteristics of the battery during charging are extracted, and the equivalent impedance of the secondary side and the steady-state parameters and efficiency of the system are calculated with great accuracy. Finally, the optimized operation curves are obtained under a wide power range. In Section IV, a 3.5 kW prototype is built. The accuracy of the proposed efficiency model is verified, the dynamic characteristics of the current closed loop are tested, and the efficiencies between the PSC and the wide-range global optimal control (WGOC) are compared over a wide power range. The applicability of the WGOC is also demonstrated. Finally, Section V concludes this article.

II. Control Method

Fig. 1 shows the schematic diagram of a double-side LCC compensated WPT system based on dual active bridges. The topology of the system contains a double-side LCC compensated resonant network and two active bridges. Among them, MOSFETs S_1–S_4 form a full-bridge inverter that converts the dc voltage Vs into a high-frequency ac square-wave voltage u_A. MOSFETs S_5–S_8 form an active rectifier that supplies power directly to

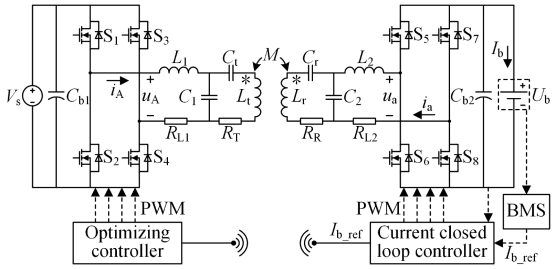

Fig. 1. Schematic of double-sided LCC type WPT system.

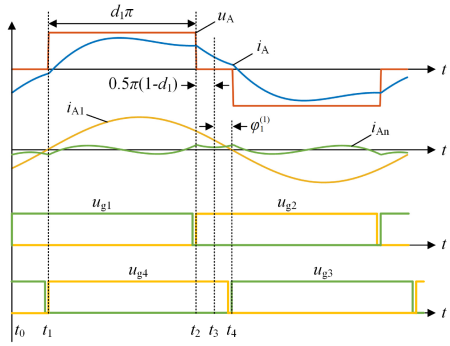

Fig. 2. Waveforms of the inverter.

the battery. In Fig. 1, L_t and L_r are the self-inductances of the transmitting and receiving coils, respectively. L_1, C_1, and C_t are the compensating elements of the transmitting coil, and L_2, C_2, and C_r are the compensating elements of the receiving coil. R_{L1}, R_{L2}, R_t, and R_r are the internal resistances of L_1, L_2, L_t, and L_r, respectively. M is the mutual inductance of the transmitting and receiving coils. In order to enhance the power transfer capability, the compensating element and the coil satisfy the resonance relationship, and the ideal resonance condition is

$$\omega_0 = \frac{1}{\sqrt{L_1 C_1}} = \frac{1}{\sqrt{L_2 C_2}} = \frac{1}{\sqrt{(L_t - L_1) C_t}} = \frac{1}{\sqrt{(L_r - L_2) C_r}} \quad (1)$$

where $\omega_0 = 2\pi f_0$, and f_0 is the resonant frequency.

A. Driving Method of Active Bridges

On the primary side, the output voltage of the inverter u_A is controlled by phase shifting. A typical waveform of the inverter is shown in Fig. 2, where u_{g1}–u_{g4} represent the driving waveforms of S_1–S_4. The d_1 is the positive duty cycle of u_A, and the phase shift angle of the inverter is $\pi(1\text{-}d_1)$. The $u_A(t)$ is obtained by Fourier expansion

$$u_A(t) \sim -\frac{4V_s}{\pi} \sum_{n=1}^{\infty} \frac{1}{n} \sin\frac{n\pi d_1}{2} \cos\left(n\omega_0 t + \frac{n\pi d_1}{2}\right). \quad (2)$$

In the active rectifier circuit on the secondary side, the driving method, as shown in Fig. 3, is adapted to take into account the output control, ZVS, and synchronous rectification. In Fig. 3,

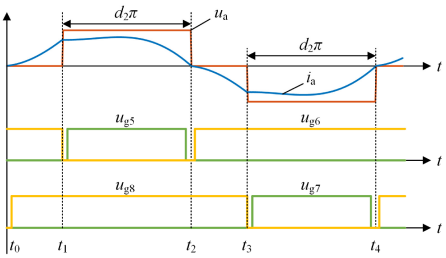

Fig. 3. Driving signal waveforms of the active rectifier.

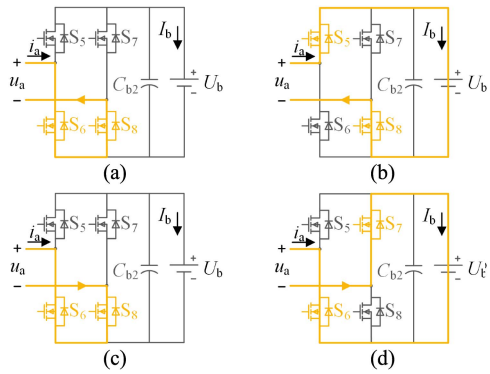

Fig. 4. Operating status of the active rectifier. (a) t_0-t_1. (b) t_1-t_2. (c) t_2-t_3. (d) t_3-t_4.

u_{g5}–u_{g8} represent the driving waveforms of S_5–S_8. The corresponding operating state is shown in Fig. 4. It is divided into four stages in one cycle.

1) t_0-t_1: S_6 conducts, and a short circuit loop is formed between S_6 and S_8.
2) t_1-t_2: S_6 is closed, the current flows from the source to S_5, and after passing through the load it flows out from the drain of S_8.
3) t_2-t_3: S_8 conducts, and a short circuit is formed between S_6 and S_8.
4) t_3-t_4: S_8 is closed, the current flows into S_7 from the source, and flows out from the drain of S_6 after passing through the load. So, the closing phase angle ($d_2\pi$) of S_6 and S_8 controls the output current of the rectifier.

This leads to the equation of I_b versus i_a

$$I_b = \frac{1}{2f_0}\int_{t_2-d_2/2f_0}^{t_2} i_a dt. \tag{3}$$

In addition, S_5 is driven at t_1-t_2 and S_6 is driven at t_2-t_4 to reduce the loss of the MOSFET during reverse conduction by synchronous rectification. Furthermore, the implementation of ZVS necessitates the assurance that the body diode is forward-conducting when driving the MOSFET. Therefore, a deadband is set after t_1 to wait for i_a to complete the commutation from S_6 to the body diode of S_5 to achieve the ZVS of S_5. Similarly, a deadband is set after t_2 to achieve the ZVS of S_6. Due to the symmetry of the full bridge circuit, S_7 and S_8 operate in the same way as S_5 and S_6. Thus, this driving method realizes ZVS and full-cycle synchronous rectification of all devices, which is extremely helpful for efficiency improvement.

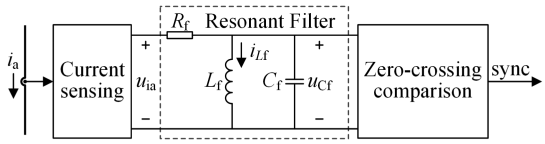

Fig. 5. Synchronization method on the secondary side.

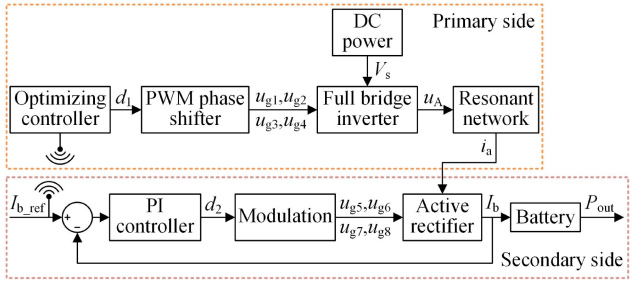

Fig. 6. Dual-sided control loop.

B. Solution for Synchronization

The driving method shown in Fig. 3 needs the synchronization signal from the primary side as a reference. A synchronization method based on a resonant filter is used and the schematic is shown in Fig. 5 [25]. The i_a is measured by a current sensor and the sensed signal is processed by a resonant filter, which is followed by a zero-crossing comparator to generate the synchronization signal sync. The components of the filter satisfy the following equation:

$$\omega_0 = \frac{1}{\sqrt{L_f C_f}}. \tag{4}$$

The transmission gain of the resonant filter is

$$G_f(\omega) = 1 - \frac{(\omega_0^2 - \omega^2)}{(\omega_0^2 - \omega^2) + j\omega_0^2 \omega L_f / R_f}. \tag{5}$$

According to (5), the filter has a gain of 1 at the resonant frequency, and the gain at the harmonic frequency decreases as L_f/R_f decreases. When L_f/R_f is small enough, almost all harmonics can be filtered so that the phase of the sync can be synchronized with the primary side.

C. Dual-Sided Control Loop

The proposed dual-side control loop of the WGOC is shown in Fig. 6. The secondary side controller sends the charging current demand I_{b_ref} given by the battery management system (BMS) to the primary side controller through wireless communication in real time. The primary side controller controls d_1 based on I_{b_ref} and outputs the corresponding drive signal to regulate u_A. A current closed loop is constructed on the secondary side, where the feedback value of I_b is obtained through the current sensor, and the PI controller adjusts d_2 according to the current error and outputs the corresponding pulsewidth modulator (PWM) signal to realize the tracking of I_{b_ref}. The current closed loop is entirely on the secondary side, which eliminates the need for wireless

communication and ensures high reliability and responsiveness. The optimal control curve of the primary side converter for a wide range of power is the key to achieving efficiency optimization of the above control loop. This is determined by accurately modeling the efficiency of the double-side LCC compensated WPT system based on the battery load characteristics.

III. Efficiency Model With Battery Load

The objective of this section is to model the efficiency of a battery-load-based wireless charging system and to determine the control curve on the primary side. This section is organized into the following three steps.

1) To consider the impedance variation of the battery under wide power, it is necessary to obtain the *R-I* characteristics of the battery based on testing.
2) Based on the *R-I* characteristics of the battery, the steady state parameters of the system, including d_2, i_{A1}, i_{a2}, I_b, I_t, and I_r, are derived with d_1 and P_o as variables.
3) The overall losses across the entire system are calculated based on the steady-state parameters. The efficiency surface about d_1 and P_o must then be obtained, after which the optimal control curve for d_1 across a wide power range is extracted.

A. R-I Characteristics of Batteries

In the actual system, the *R-I* characteristics of the battery can be obtained from the charging curve. This part presents an illustrative example using NCR18650BD cells, demonstrating how the *R-I* characteristics of the battery package can be derived from the results of a single cell's charging test. The NCR18650BD has a rated capacity of 2980 mAh, a rated voltage of 3.6 V, and a recommended maximum charging current of 909 mA at temperatures between 10 °C and 45 °C. To facilitate experimental validation, the simulated battery package is sized as 44 stages in series and 26 stages in parallel, with a rated voltage of 158.4 V and a rated capacity of 77.48 Ah. The power rating of the system is set at 3.5 kW. Fig. 7(a) presents the voltages observed for a single cell subjected to a charge rate of 0.1 A–1.5 A (0.03C to 0.5C) at low and high charge levels, respectively. Based on these observations, the *R-I* curve of the simulated battery pack is calculated and presented in Fig. 7(b). It can be seen that the *R-I* curves at high and low charges are highly proximate, thus, the mean is employed for subsequent calculations. A power function is fitted to the mean data, and the fitted function is

$$R_b = 160.6 I_b^{-1} + 0.1898. \tag{6}$$

The fitted curve is illustrated in Fig. 7(c). The sum of the squared errors (SSE) represents a crucial metric for evaluating the quality of the fitting results. The SSE is calculated as follows:

$$\mathrm{SSE} = \sum_{i=1}^{n} w_i (y_i - \hat{y}_i)^2. \tag{7}$$

The SSE of the fitting result is 0.0001704, which indicates that (6) fits well with the measurement results. The equation of

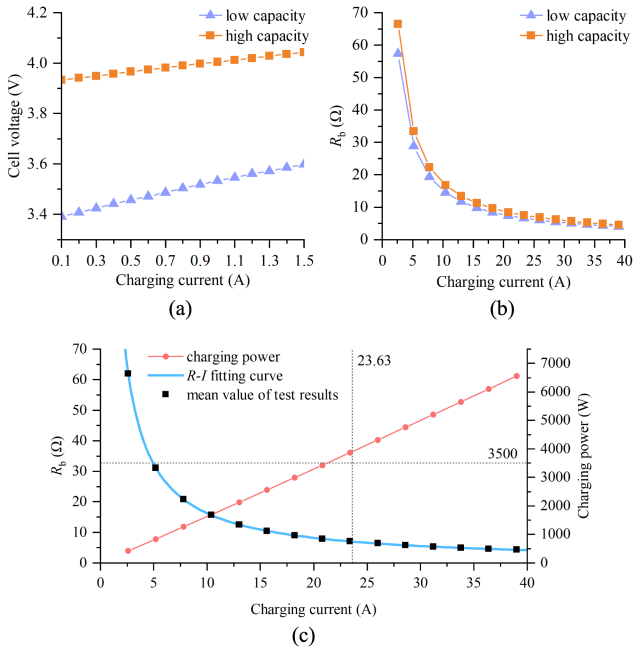

Fig. 7. Battery charging characteristics.

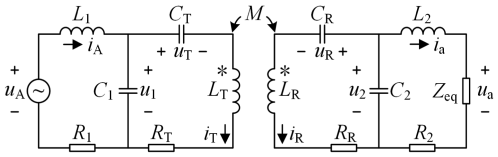

Fig. 8. Equivalent circuit of double-sided LCC type WPT system.

I_b and P_o can be derived from (6)

$$I_b^2 R_b(I_b) = P_o. \tag{8}$$

Fig. 7(c) gives the power curve of the battery package. In addition, the recommended maximum charging current of the battery package is calculated based on the number of parallel stages as 23.63 A. It can be observed in Fig. 7(c) that the charging current at a power of 3.5 kW is below the recommended maximum charging current. This indicates that the simulated battery package complies with the recommended operating region.

It is important to note that the aforementioned simulation method can also be employed for other packages and cell sizes.

B. Calculation of Steady State Parameters

In order to model the efficiency, expressions for the steady state parameters of the system concerning P_o and d_1 are derived based on the constraints of (8). The inverter is equated to an ac power supply, the active rectifier and the battery are equated to Z_{eq}, and the ON-state resistance of the active bridge is equated to R_{AB}. The equivalent circuit of the system is shown in Fig. 8, where $R_1 = R_{L1} + R_{AB}$ and $R_2 = R_{L2} + R_{AB}$. The input

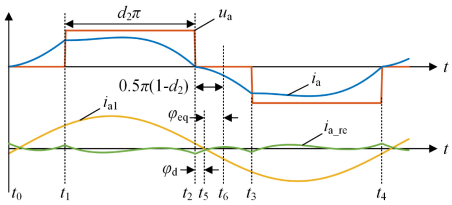

Fig. 9. Typical operating waveforms of the active rectifier.

impedance Z_1 of the resonant network is

$$\begin{cases} Z_{22} = j\omega L_r + R_r + \frac{1}{j\omega C_r} + \frac{1}{j\omega C_2 + \frac{1}{j\omega L_2 + R_2 + Z_{eq}}} \\ Z_{21} = \frac{M^2\omega^2}{Z_{22}} \\ Z_1 = R_1 + j\omega L_1 + \frac{1}{j\omega C_1 + \frac{1}{j\omega L_t + \frac{1}{j\omega C_t} + Z_{21} + R_t}}. \end{cases} \tag{9}$$

Based on (2) and (9), i_A can be obtained by

$$i_A(t) \sim -\frac{4V_s}{\pi}\sum_{n=1}^{\infty}\frac{1}{n\left|Z_1^{(n)}\right|}\sin\frac{n\pi d_1}{2}\cos\left(n\omega_0 t + \frac{n\pi d_1}{2} - \varphi_1^{(n)}\right) \tag{10}$$

where $Z^{(n)}{}_1 = Z_1(n\omega_0)$, $\varphi^{(n)}{}_1$ is the impedance angle of $Z^{(n)}{}_1$, $n = 1, 3, 5\ldots$.

The waveform of i_A is illustrated in Fig. 2. i_{A1} represents the fundamental current, while i_{An} denotes the sum of harmonic currents. t_4 is the zero-crossing point of i_{A1}. The power factor angle of the fundamental wave at the output of the inverter is designated as $\varphi^{(1)}{}_1$. In (9), Z_{eq} is the variable that follows the operating state of the circuit and therefore requires determination with priority. Due to the phenomenon of resonance, the transmission of harmonic power to the secondary side is minimal. Consequently, the calculation of the fundamental impedance $Z^{(1)}{}_{eq}$ is sufficient

$$Z_{eq}^{(1)} = \frac{U_{a1}}{I_{a1}}e^{j\varphi_{eq}} \tag{11}$$

where U_{a1} is the fundamental amplitude of u_a, I_{a1} is the fundamental amplitude of i_a, and φ_{eq} is the fundamental power factor angle of the active rectifier.

The typical operating waveforms of the active rectifier are shown in Fig. 9. Due to the effect of dc bus capacitance, u_a presents as a square wave or a step wave. According to Fig. 9, u_a is derived by the Fourier series expansion

$$u_a(t) \sim -\frac{4I_bR_b}{\pi}\sum_{n=1}^{\infty}\frac{1}{n}\sin\frac{n\pi d_2}{2}\cos\left(n\omega_0 t + \frac{n\pi d_2}{2}\right) \tag{12}$$

where $n = 1, 3, 5\ldots$.

The i_a is divided into two parts: i_{a1}, which is transmitted from the primary side, and i_{a_re}, which is excited by u_a in the resonant network [23]. Thus

$$i_a = i_{a1} + i_{a\_re}. \tag{13}$$

Due to the significant attenuation of harmonics by the resonant network, i_{a1} contains solely the fundamental waveform. When the resonance condition is satisfied and the internal resistance of the coils and the inductors are not considered, I_{a1} can be calculated by

$$I_{a1} = \frac{4V_sM}{\pi\omega_0 L_1 L_2}\sin\frac{\pi d_1}{2}. \tag{14}$$

Subsequently, to calculate i_{a_re}, the input impedance of the secondary side of the resonant network Z_2 is determined. According to Fig. 8, Z_2 can be obtained by

$$\begin{cases} Z_{11} = j\omega L_t + R_t + \frac{1}{j\omega C_t} + \frac{1}{j\omega C_1 + \frac{1}{j\omega L_1 + R_1}} \\ Z_{12} = \frac{M^2\omega^2}{Z_{11}} \\ Z_2 = R_2 + j\omega L_2 + \frac{1}{j\omega C_2 + \frac{1}{j\omega L_r + \frac{1}{j\omega C_r} + Z_{12} + R_r}}. \end{cases} \tag{15}$$

Based on (12) and (15), i_{a_re} can be obtained by

$$i_{a\_re}(t) \sim -\frac{4I_bR_b}{\pi}\sum_{n=1}^{\infty}\frac{1}{n\left|Z_2^{(n)}\right|}\sin\frac{n\pi d_2}{2}\cos\left(n\omega_0 t + \frac{n\pi d_2}{2} - \varphi_2^{(n)}\right) \tag{16}$$

where $Z^{(n)}{}_2 = Z_2(n\omega_0)$, $\varphi^{(n)}{}_2$ is the impedance angle of $Z^{(n)}{}_2$, $n = 1, 3, 5\ldots$.

From Fig. 9, it can be seen that since i_{a_re} is not negligible, the zero-crossing point of $u_a(t_2)$ must be ahead of the zero-crossing point of $i_{a1}(t_5)$. At t_2 there is

$$i_a(t_2) = 0. \tag{17}$$

And

$$i_{a\_re}(t_2) = i_{a\_re}\left(\frac{\pi}{\omega_0}\right). \tag{18}$$

Combining (17) and (18), the phase difference φ_d between t_2 and t_5 can be calculated by the inverse trigonometric function

$$\varphi_d = -\arcsin\frac{i_{a\_re}(\pi/\omega_0)}{I_{a1}}. \tag{19}$$

Then

$$i_{a1} = I_{a1}\sin(\omega_0 t - \varphi_d). \tag{20}$$

With t_6 as the u_a fundamental zero crossing point and a phase difference of $0.5\pi(1\text{-}d_2)$ between t_2 and t_6, the power factor angle φ_{eq} of the input of the active rectifier can be calculated by

$$\varphi_{eq} = 0.5\pi(1 - d_2) + \arcsin\frac{i_{a\_re}(\pi/\omega_0)}{I_{a1}}. \tag{21}$$

Combining (11), (12), and (21), there is

$$Z_{eq}^{(1)} = \frac{4I_bR_b}{\pi I_{a1}}\sin\frac{\pi d_2}{2}e^{j\varphi_{eq}}. \tag{22}$$

In (22), d_2 is obtained through (3). According to (13) and (3) can be rephrased as

$$I_b = \frac{1}{2f_0}\left(\int_{t_2 - d_2/2f_0}^{t_2} i_{a1}dt + \int_{t_2 - d_2/2f_0}^{t_2} i_{a\_re}dt\right). \tag{23}$$

In the actual system, since R_1, R_2, R_t, and R_r are very small, Z_2 is very large at the resonance frequency, and the impedance angle of Z_2 at the harmonic frequency is nearly 90°. Consequently, the integral of i_{a_re} from t_1 to t_2 is almost 0. Therefore, (23) can be simplified as

$$I_b = \frac{I_{a1}}{\pi}(1 - \cos \pi d_2). \tag{24}$$

Furthermore, d_2 can be obtained by

$$d_2 = \frac{\arcsin(1 - \pi I_b / I_{a1})}{\pi}, \quad I_{a1} \geq 0.5\pi I_b. \tag{25}$$

Up to this point, the values of i_A, d_2, and i_a in steady state can be calculated from the determined values of V_s, d_1, and P_o.

C. Parameter Corrections at Nonideal Resonance

It is important to note that (14) is based on ideal conditions. To achieve high accuracy in the model, it is necessary to consider the effect of internal resistance and deviation of component parameters in the actual system. Therefore, expressions based on actual component parameters are derived.

According to Fig. 8, the system of Kirchhoff equations for the system is listed as

Based on (26) shown at the bottom of the this page, I_{a1}, I_t, and I_r can be derived as

$$\dot{I}_{a1} = j\frac{4\omega_0 M V_s}{\pi Z_A Z_B} \sin \frac{\pi d_1}{2} \tag{27}$$

$$I_t = \left| \frac{\frac{4V_s}{\pi} \sin \frac{\pi d_1}{2} + j\omega_0 M \left(1 + \frac{Z_{L1}}{Z_{C1}}\right)\left(1 + \frac{Z_{L2}+Z_{eq}}{Z_{C2}}\right) \dot{I}_{a1}}{Z_A} \right| \tag{28}$$

$$I_r = \frac{\omega_0 M}{|Z_{22}(\omega_0)|} I_t \tag{29}$$

where

$$Z_{L1} = j\omega_0 L_1 + R_1, Z_{L2} = j\omega_0 L_2 + R_2 \tag{30}$$

$$Z_{Lt} = j\omega_0 L_t + R_t, Z_{Lr} = j\omega_0 L_r + R_r \tag{31}$$

$$Z_A = Z_{L1} + \left(1 + \frac{Z_{L1}}{Z_{C1}}\right)(Z_{Lt} + Z_{Ct}) \tag{32}$$

$$Z_B = Z_{eq} + Z_{L2} + (Z_{Lr} + Z_{Cr})\left(1 + \frac{Z_{L2} + Z_{eq}}{Z_{C2}}\right) + \frac{\omega_0^2 M^2 \left(1 + \frac{Z_{L1}}{Z_{C1}}\right)\left(1 + \frac{Z_{L2}+Z_{eq}}{Z_{C2}}\right)}{Z_A}. \tag{33}$$

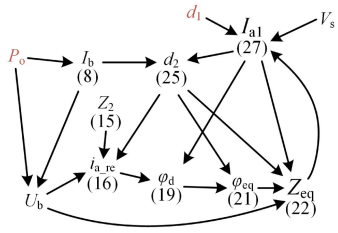

Fig. 10. Relationship diagram for I_{a1} and Z_{eq}.

The conjunction of (22) with (27) leads to the inference that the variables I_{a1} and Z_{eq} are correlated. Based on the aforementioned derivation, the interrelationship of the variables is illustrated in Fig. 10. Given that I_{a1} and Z_{eq} are variables of each other, it is not possible to provide equations for I_{a1} and Z_{eq} concerning d_1 and P_o. Consequently, an iterative calculation method is employed to approximate the exact values. A flowchart, as illustrated in Fig. 11, has been designed with the following running process.

1) Calculate I_{a1} based on (14) and use it as the initial value.
2) Determine whether $I_{a1} \geq 0.5\pi I_b$ is satisfied. If it is, the current I_{a1} is assigned to I_{a1}'.
3) Substitute I_{a1} into a series of equations, as shown in Fig. 10, and compute new I_{a1}.
4) If the error rate between I_{a1}' and I_{a1} is less than ε, the loop is exited. Otherwise, steps 2), 3), and 4) are repeated.
5) After the loop, I_{a1}, i_{a_re}, Z_{eq}, and d_2 are determined, and subsequently, i_A, i_a, I_t, and I_r are computed according to (10), (13), (28), and (29), respectively.

D. Method for Obtaining the Optimal Curve

In order to obtain the optimal curve, the efficiency is calculated for a wide operating range based on the steady-state parameters. The main considerations are coil losses, compensating inductor losses, conduction losses, and switching losses of the active bridge. The total losses of the system can be expressed as

$$P_{loss} = 0.5I_t^2 R_t + 0.5I_r^2 R_r + I_{A\_rms}^2 R_1 + I_{a\_rms}^2 R_2 + P_{sw} \tag{34}$$

where P_{sw} represents the switching loss of the active bridge.

$$\begin{bmatrix} \dot{U}_A \\ \dot{U}_1 \\ \dot{I}_t \\ \dot{I}_A \\ \dot{U}_a \\ \dot{U}_2 \\ \dot{I}_r \\ \dot{I}_a \end{bmatrix} = \begin{bmatrix} j\omega L_1 + R_1 & 1 & & & & & & \\ 0 & 0 & j\omega L_t + R_t & 1 & & & & \\ & & & j\omega C_t & & & & \\ & j\omega C_1 & 1 & & & & & \\ & & & & & j\omega M & & \\ & & j\omega M & & -j\omega L_2 - R_2 & 1 & & \\ & & & & & & j\omega L_r + R_r & 1 \\ & & & & & & & j\omega C_r \\ & & & & & -j\omega C_2 & -1 & \end{bmatrix} \begin{bmatrix} \dot{I}_A \\ \dot{U}_1 \\ \dot{I}_t \\ \dot{U}_t \\ \dot{I}_a \\ \dot{U}_2 \\ \dot{I}_r \\ \dot{U}_r \end{bmatrix}. \tag{26}$$

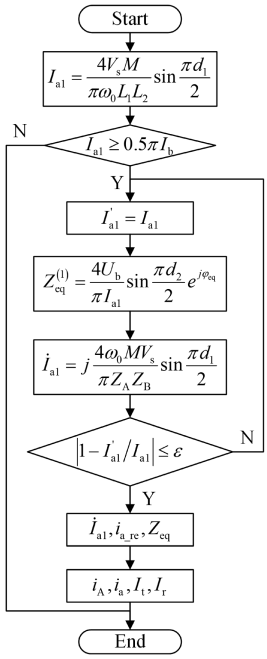

Fig. 11. Iteration flowchart.

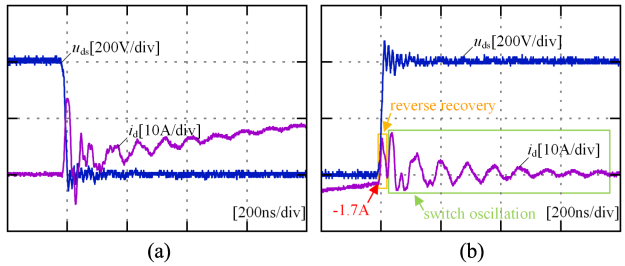

Fig. 12. Waveforms of S_3 and S_4 when hard-switching. (a) Turn-ON process. (b) Turn-OFF process.

TABLE I
PARAMETERS OF THE CIRCUIT

Symbol	Parameter	Value
V_s	Voltage of the dc source	400 V
R_{AB}	On-state resistance of the active bridge	0.115 Ω
L_t	Primary side coil inductance	96.35 μH
L_r	Secondary side coil inductance	90.60 μH
R_t	Internal resistance of L_t	0.195 Ω
R_r	Internal resistance of L_r	0.203 Ω
L_1	Primary side compensated inductance	20.7 μH
R_{L1}	Internal resistance of L_1	0.048 Ω
L_2	Secondary side compensated inductance	12.9 μH
R_{L2}	Internal resistance of L_2	0.034 Ω
C_1	Primary side compensation capacitor	155.1 nF
C_2	Secondary side compensation capacitor	257.9 nF
C_t	Primary side resonant capacitor	43.5 nF
C_r	Secondary side resonant capacitor	42.0 nF
f_0	Resonant frequency	88.106 kHz
M	Mutual inductance	10.1 μH
k	Coupling coefficient	0.108

In (34), R_t, R_r, R_1, and R_2 are measured by the LCR meter. I_t, I_r, and the time-domain expressions for i_A and i_a are accurately calculated according to Fig. 11. $I_{A\cdot rms}$ and $I_{a\cdot rms}$ are further obtained by root-mean-square computation of the time-domain values.

On the secondary side, ZVS is realized for all devices, and the turn-OFF time of the MOSFET is very short. Thus, the switching losses of the active rectifier can be ignored [22]. On the primary side, the switching losses are calculated based on ZVS states. In accordance with the principle of ZVS, the primary side inverter is capable of achieving ZVS under the following conditions:

$$\begin{cases} i_A(t_1) < 0 \\ i_A(t_2) > 0 \end{cases}. \tag{35}$$

It should be noted that (35) is not necessarily satisfied in all operating states. In the event that ZVS cannot be realized, it is important to consider the hard-switching loss and reverse recovery loss of the body diode. To facilitate a more accurate estimation of the hard-switching loss, an experimental approach is employed to establish an estimation formula. The model number of the MOSFET employed in the prototype is C3M0045065K. The current of the device is measured by the Rogowski coil. Fig. 12 presents the measured voltage and current waveforms during hard switching. With regard to the turn-ON process depicted in Fig. 12(a), the hard turn-ON loss P_{ON} is theoretically linearly related to the turn-OFF current, given that V_s is fixed in this system. With regard to the turn-OFF process, as illustrated in Fig. 12(b), it can be divided into two distinct phases: 1) reverse recovery and 2) oscillation. During the reverse recovery phase, the reverse recovery loss P_{re} is found to be linearly related to the turn-OFF current. In contrast, the oscillation phase is characterized by a loss P_{osc} that is dependent on the turn-OFF voltage rather than the turn-OFF current. Therefore, in combination with (35), the switching loss of the primary side inverter is calculated by the following equation:

$$P_{sw}(t_1) = \begin{cases} k_{hsw} i_A(t_1) + P_{osc}, & i_A(t_1) > 0 \\ 0, & i_A(t_1) \leq 0 \end{cases} \tag{36}$$

$$P_{sw}(t_2) = \begin{cases} -k_{hsw} i_A(t_2) + P_{osc}, & i_A(t_2) < 0 \\ 0, & i_A(t_2) \geq 0 \end{cases} \tag{37}$$

where k_{hsw} is the hard-switching loss coefficient, $k_{hsw} = (P_{ON} + P_{re}) / i_A(t_{sw})$, and P_{osc} is the oscillation loss.

In the test shown in Fig. 12, $P_{ON} = 2.39$ W, $P_{re} = 4.55$ W, $P_{osc} = 14$ W, and the current at the instant before switching is 1.7 A. So that $k_{hsw} = 4.08$.

In summary, based on i_A, i_a, I_t, I_r, P_{sw}, and (34), the efficiency of the system can be obtained

$$\eta \approx \frac{P_o}{P_o + P_{loss}}. \tag{38}$$

According to (34), the loss breakdown can be calculated. The parameters of the power supply and circuit are presented in Table I. The loss breakdown at $P_o = 3.5$ kW is shown in Fig. 13, where $P_{loss} = 388.8$ W, and $\eta = 90\%$.

In order to ascertain the efficiency in the d_1-P_o plane, a parameter scan is conducted for (38). The value of d_1 is varied from 0.1 to 1 in increments of 0.01, while that of P_o is varied from 0.5 kW to 3.5 kW in increments of 0.2 kW. And the

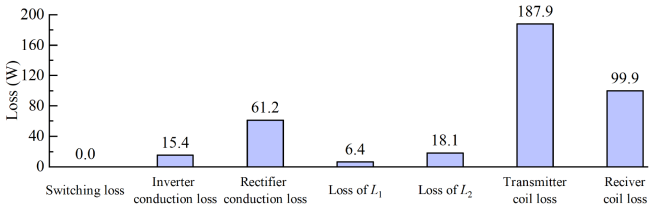

Fig. 13. Loss breakdown at $P_o = 3.5$ kW.

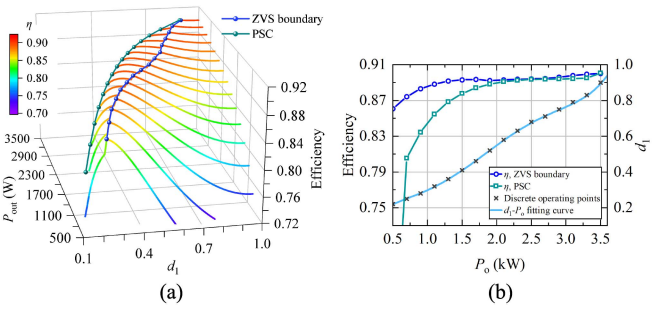

Fig. 14. Optimization results. (a) Results of the efficiency model. (b) Fitting curve of operating points.

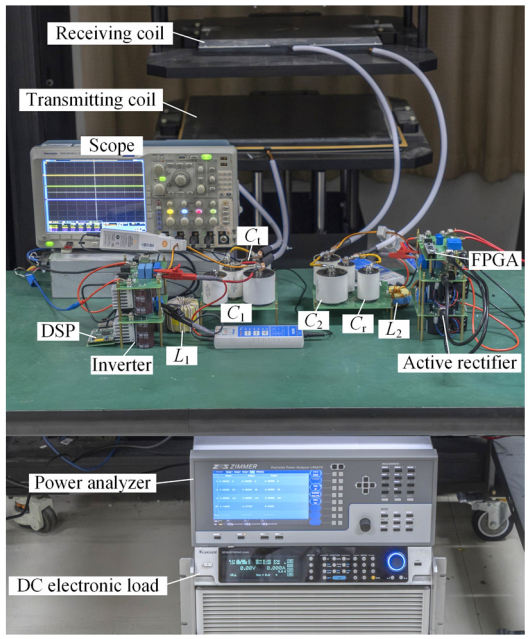

Fig. 15. Photograph of the experimental prototype.

ε in Fig. 11 is set to 0.001. The efficiency results are shown in Fig. 14(a), which clearly illustrates the pattern of change in efficiency when varying d_1 at each power level. The operating trajectory of the PSC exhibits a notable decline in efficiency as power levels decline. The dual active bridge-based system, however, is capable of adjusting the operating point to the region of high efficiency by adjusting d_1 and d_2. In accordance with (35), the ZVS boundary is indicated in Fig. 14(a). ZVS can be fully realized in the primary side inverter on the right side of the boundary. Fig. 14(b) shows the efficiency comparison in a two-dimensional view. It is evident that the efficiency can be enhanced by operating on the ZVS boundary in comparison to the PSC. A function of $d_1(P_o)$ is fitted based on discrete ZVS boundary data. The MATLAB Curve Fitting Toolbox is employed for this purpose. It is found that a five-times function achieves good fitting results. The function to fit the curve is as follows:

$$f(x) = 0.01822x^5 - 0.1656x^4 + 0.5301x^3 - 0.698x^2 + 0.5527x + 0.061. \quad (39)$$

The SSE of the fitting result is 0.0001014, and the curve is shown in Fig. 14(b). Up to this point, the control function for the optimized efficiency of the primary side inverter is obtained. Based on this function, the proposed WGOC can regulate the system to the optimal operating point in the full power range.

IV. Experimental Verification

In order to verify the effectiveness of the proposed efficiency model and optimization strategy, a prototype is built, as shown in Fig. 15. The prototype contains a dc source, a full-bridge inverter, an active rectifier, an electronic load, a double-side LCC compensation network, and coupling coils. The schematic diagram of the prototype is shown in Fig. 1, and the parameters of the components are shown in Table I. The coupling coils are of planar helical structure and each coil consists of Litz wire, ferrite cores, an aluminum plate, and a plastic frame. The parameters of the coupling coils are given in Table II. The dielectric of the compensation capacitor is polypropylene film and the detailed parameters of the capacitor are given in Table III.

The power devices of the active bridge are SiC MOSFETs (C3M0045065K from CREE). The primary side inverter is controlled by a DSP (TMS320F28379D from TI) and the secondary side active rectifier is controlled by an FPGA (XC7A35T from Xilinx). The system efficiency is measured by a power

TABLE II
Parameters of the Coupling Coils

Parameter	Value
Size of L_T	500 mm × 500 mm
Size of L_R	400 mm × 400 mm
Turns of the L_T	10
Turns of the L_R	16
Spacing between turns	3.5 mm
Number of strands of Litz wire	1800
Single strand diameter of Litz wire	0.10 mm
Distance between coupling coils	200 mm
Ferrite core material	PC95
Size of single ferrite core	100 mm×100 mm ×10 mm

TABLE III
Parameters of the Compensation Capacitors

Parameter	Value
U_{rms}	3000 V
I_{rms}	40 A
d_v/d_t	3500 V/μs
ESR@1.0kHz	2 mΩ

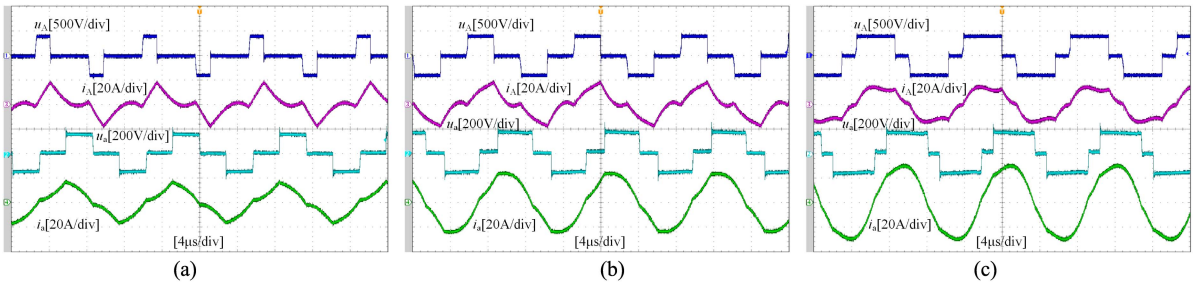

Fig. 16. Experimental waveforms. (a) $P_o = 900$ W. (b) $P_o = 1900$ W. (c) $P_o = 2900$ W.

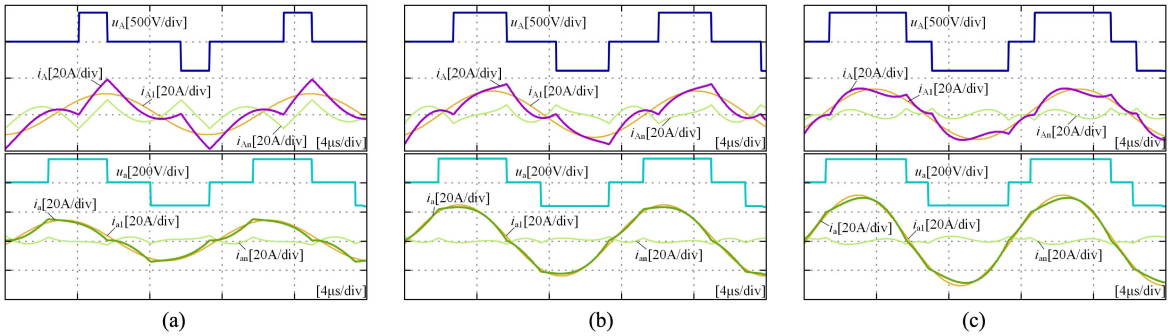

Fig. 17. Waveforms computed by the parametric model. (a) $P_o = 900$ W. (b) $P_o = 1900$ W. (c) $P_o = 2900$ W.

TABLE IV
PARAMETERS OF THE SYNCHRONIZATION CIRCUIT

Parameter	Value
L_f	100 μH
C_f	32.63 nF
R_f	10 kΩ
Part number of the current sensor	LAH 50-P/SP1
Part number of the comparator	TLV3201AIDBV

TABLE V
COMPARISON OF EXPERIMENTAL AND MODELLED EFFICIENCIES

P_o	d_1	d_2	Load resistance	Efficiency (prototype)	Efficiency (model)	Inaccuracy
900 W	0.28	0.58	29 Ω	86.9%	88.1%	1.38%
1900 W	0.52	0.67	14 Ω	88.4%	89.5%	1.24%
2900 W	0.75	0.79	9 Ω	88.8%	89.8%	1.13%

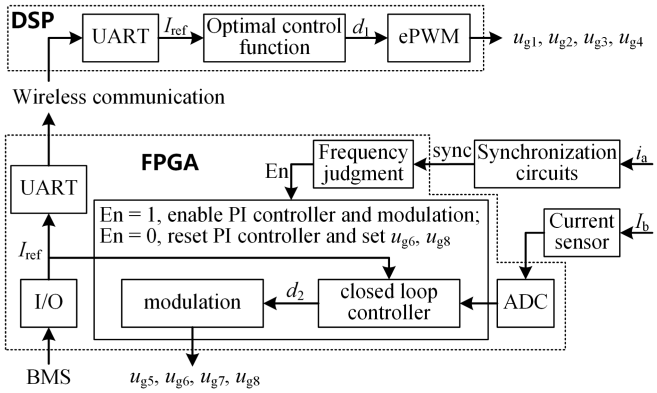

Fig. 18. Functional diagram of the processors.

analyzer (LMG670 from GMC-I). The device parameters of the synchronization circuit are shown in Table IV.

A. Efficiency Model Verification

The results of the model and experiments are compared to verify the accuracy of the model. Three test points with power 900 W, 1900 W, and 2900 W are selected on the ZVS boundary. The experimental parameters of the test points are shown in Table V. Fig. 16 presents the experimental waveforms of these three test points. Fig. 17 presents the waveforms calculated by the model. A comparison of Figs. 16 and 17 reveals a high degree of consistency between the measured and calculated waveforms. This indicates that the parametric model is able to accurately represent the operational state of the actual system. Furthermore, the experimental and modeled efficiencies are compared in Table V, and the error in the model's estimated efficiency is calculated. The average error of the model is 1.25%. This is an acceptable error rate, given that the loss of hard shutdown is not considered in the model. In conclusion, the experiment demonstrates that the efficiency model has high accuracy.

B. Optimization Strategy Verification

In order to verify the effectiveness of the secondary side current closed loop, load disturbance tests, and primary side disturbance tests are performed. The functional diagram of the processors shown in Fig. 18 is designed. In the primary side DSP, u_{g1}–u_{g4} are generated by the enhanced PWM peripheral. The value of I_{ref} is also received through the UART port and d_1

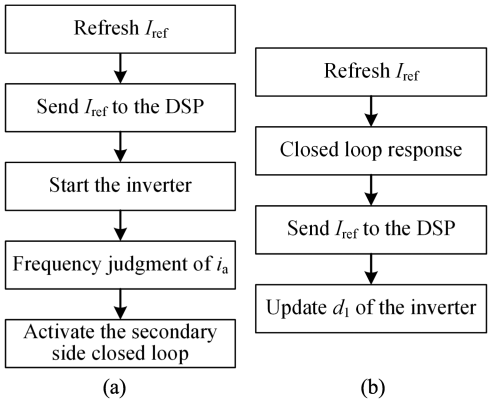

Fig. 19. Control system process. (a) Initial stage of charging. (b) Response to changes in I_{ref}.

is adjusted according to the optimal control function. I_{ref} does not change at high frequency during charging and efficiency optimization does not require an immediate response when I_{ref} changes. Therefore, the primary side control does not need to set a high sampling frequency. In the experiment, the sampling time of the primary side control is 5s. In the FPGA on the secondary side, several parallel modules are implemented: an analog-to-digital converter, a closed-loop controller, a modulator, and a frequency discriminator. The closed-loop controller receives I_b and I_{ref} and outputs d_2 after a discrete PI operation. The modulator generates the corresponding u_{g5}–u_{g8} based on d_2. The frequency discriminator calculates the frequency of the synchronization signal *sync* in real-time and outputs *En*, which is set when the frequency is correct and reset when opposite. The closed-loop controller and modulator are enabled by the *En* signal. When $En = 0$, resets the PI controller and sets u_{g6}, u_{g8} to short-circuit the input to the rectifier thus turning off the output. When $En = 1$, the closed-loop controller and modulator are enabled. Based on the designed control logic, the flow of the system at startup is shown in Fig. 19(a). First, after recognizing the charging request, the FPGA sends I_{ref} to the DSP, then the DSP turns ON the inverter and the secondary side generates an induced current. Subsequently, the FPGA recognizes the correct frequency of i_a and starts the closed loop on the secondary side. During operation, when the I_{ref} changes, the system response flow is shown in Fig. 19(b). After the I_{ref} is refreshed, the secondary side closed loop responds immediately, and then the FPGA sends the I_{ref} to the DSP. Subsequently, the DSP adjusts d_1 to complete the operation point optimization. The output current sensor is the CAS 50-NP from LEM, with a sensitivity of 12.5 mV/A. In the experiment, the PI controller is implemented in discrete form by FPGA, and the output of step m is

$$u(m) = k_p [e(m) - e(m-1)] + k_i T_s e(m) + u(m-1) \tag{40}$$

where $T_s = 10\ \mu s$, $k_p = 0.5$, $k_i = 100$.

The waveforms of the soft switching for the active rectifier were measured, as shown in Fig. 20. The turn-ON signal of S5 is set with a 150 ns deadband to wait for the junction capacitor to discharge. The turn-ON signal of S6 is given by the FPGA after

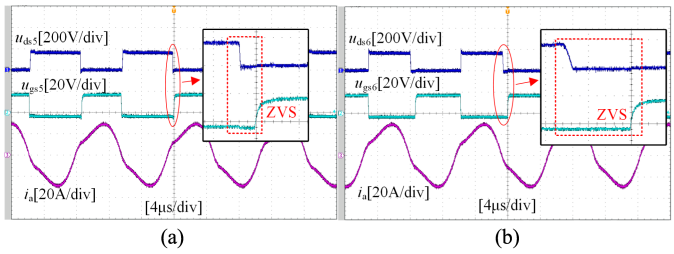

Fig. 20. Waveforms of the soft switching for the active rectifier. (a) ZVS of S_5. (b) ZVS of S_6.

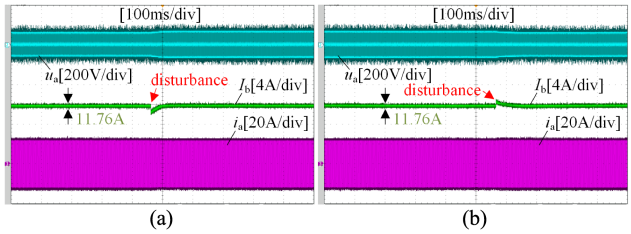

Fig. 21. Load disturbances test. (a) From 9 Ω to 11 Ω. (b) From 11 Ω to 9 Ω.

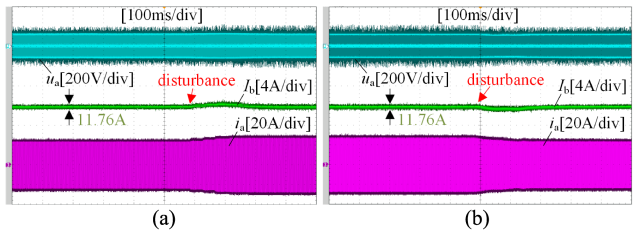

Fig. 22. Primary side disturbances test. (a) d_1 from 0.52 to 0.59. (b) d_1 from 0.59 to 0.52.

detecting the zero-crossing signal of i_{a1}. Due to symmetry, S7 and S8 can also realize ZVS. The experiment demonstrates that soft switching can be reliably implemented in active rectifiers.

For the load perturbation test, the value of d_1 is set to 0.52, while the value of I_{b_ref} is set to 11.66 A. Fig. 21(a) illustrates the waveforms that are generated when the load is suddenly increased from 9 Ω to 11 Ω. It can be observed that I_b remains stable prior to the introduction of the perturbation input. At the moment of load increase, I_b experiences a decline due to the inability of the voltage of the C_{b2} to change abruptly. This is followed by a return to the steady state within 40 ms, as a result of the action of the current loop. Fig. 21(b) illustrates the waveforms of the load transitioning from 11 Ω to 9 Ω. Similarly, there is a jump in I_b at the moment of load reduction, followed by a rapid return to a steady state.

In the primary-side perturbation test, the load is set to 9 Ω, and I_{b_ref} is still set to 11.66 A. Fig. 22(a) illustrates the waveforms when d_1 changes from 0.52 to 0.59. I_b exhibits a slight increase as i_a increases after the perturbation input, and then I_b returns to a steady state as the current loop reduces d_2. Conversely, when d_1 changes from 0.59 to 0.52, the opposite phenomenon is observed, as illustrated in Fig. 22(b).

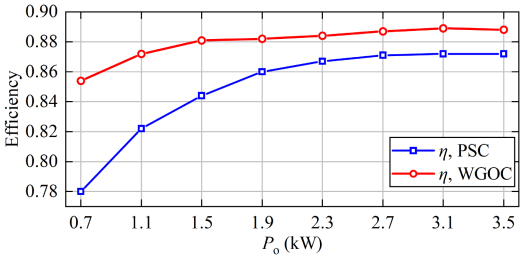

Fig. 23. Measured efficiencies of the WPT system with two control strategies.

TABLE VI
PARAMETERS OF THE WPT SYSTEM BASED ON SAE J2954

Symbol	Parameter	Value
L_t	Primary side coil inductance	45.11 μH
L_r	Secondary side coil inductance	42.57 μH
R_t	Internal resistance of L_t	0.029 Ω
R_r	Internal resistance of L_r	0.065 Ω
L_1	Primary side compensated inductance	14.7 μH
R_{L1}	Internal resistance of L_1	0.036 Ω
L_2	Secondary side compensated inductance	9 μH
R_{L2}	Internal resistance of L_2	0.022 Ω
C_1	Primary side compensation capacitor	222.0 nF
C_2	Secondary side compensation capacitor	362.6 nF
C_t	Primary side resonant capacitor	107.3 nF
C_r	Secondary side resonant capacitor	97.2 nF
f_0	Resonant frequency	88.106 kHz
d	Face-to-face distance of coils	200 mm
M	Mutual inductance	4.93 μH
k	Coupling coefficient	0.113

The experiments demonstrate that the designed secondary-side current loop is capable of achieving the target current and maintaining it in a stable state. Furthermore, the control loop is able to rapidly regulate I_b back to a steady state in the event of load disturbances and primary side disturbances.

In order to verify the effectiveness of the proposed optimal control strategy for improving efficiency, the wide power range efficiency of the PSC and the WGOC are tested separately. For the PSC test, diodes (C3D30065D from CREE) are used for the secondary side rectifier bridge. A comparison of the measured efficiencies is presented in Fig. 23. It can be observed that the optimal control strategy enhances the efficiency over the entire power range, particularly in the interval of power less than 1.9 kW, where the efficiency improvement is more pronounced, reaching up to 9.5%. Thus far, the output control and efficiency optimization of the WGOC have been verified experimentally.

In order to verify the applicability of the WGOC for different resonance parameters, another system based on the society of automotive engineers (SAE) standard is analyzed. Table VI gives the parameters of the coupling coils and their compensation networks, which are designed in accordance with the SAE standard. The primary side and secondary side coils of the system are designed with GA WPT2 and VA WPT2/Z2 given by SAE J2954 standard as reference, respectively. Substituting Table VI into the proposed efficiency model, the corresponding results are shown in Fig. 24(a). The proposed dual-side control loop enables the system to operate on the optimal path, thereby maximizing efficiency. Fig. 24(b) illustrates the control curves

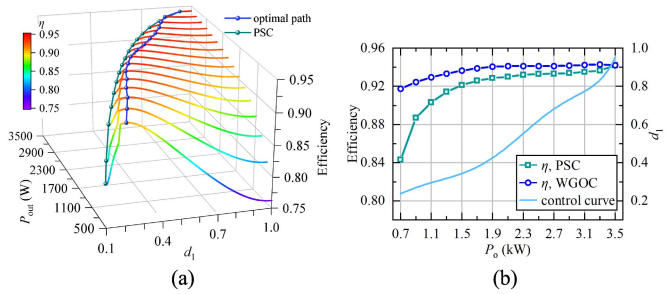

Fig. 24. Optimization results of the WPT system based on SAE J2954. (a) Efficiency model. (b) Comparison of efficiency and optimal control curves.

under the optimal strategy and compares the efficiency between the optimal path and the PSC. The function of the control curve is

$$f(x) = 0.02956x^6 - 0.321x^5 + 1.335x^4 - 2.669x^3 + 2.695x^2 - 1.167x + 0.38. \quad (41)$$

It can be seen that the optimal path achieves higher efficiency throughout the power range, improving efficiency to 91.7%-94.3%, and the optimization effect is more pronounced in the low power range. The above results verify the applicability of the WGOC in double-side LCC systems.

V. CONCLUSION

This article presents a global optimal control method for electric vehicle wireless charging systems, which is designed to enhance efficiency over a wide power range. The driving method for implementing ZVS and full-cycle synchronous rectification for all devices of the active rectifier is presented. The enhanced dual-sided control loop, comprising a current loop on the secondary side and an efficiency optimization loop on the primary side, is presented. In order to obtain the target curve for optimal control of the primary side, the double-sided LCC system is taken as an example to establish an efficiency model based on the battery load. The impedance characteristics of an EV battery pack are simulated based on the results of cell tests. The zero-crossing point offset of the secondary side current is analyzed, and the equivalent impedance of the secondary side is derived. The steady-state operating parameters of the system are calculated with great precision. The efficiency in the d_1-P_o plane is analyzed based on the soft-switching case of the dual active bridges and a function of the optimal operating point is fitted. A 3.5 kW prototype was built to verify the effectiveness of the WGOC. The accuracy of the efficiency model is experimentally verified. Meanwhile, compared with the PSC, the proposed WGOC improves the efficiency in the full power range. In addition, the optimization effect is examined in another double-sided LCC system based on the SAE standard, which proves the applicability of the proposed method. At present, the optimal control curve is dependent on the accuracy of the system parameters. Subsequent studies will investigate the effect of mutual inductance variations in coupled coils and autonomous identification methods for mutual inductance.

REFERENCES

[1] P. Machura, V. De Santis, and Q. Li, "Driving range of electric vehicles charged by wireless power transfer," *IEEE Trans. Veh. Technol.*, vol. 69, no. 6, pp. 5968–5982, Jun. 2020.

[2] Z. Deng et al., "Design of a 60-kW EV dynamic wireless power transfer system with dual transmitters and dual receivers," *IEEE J. Emerg. Sel. Topics Power Electron.*, vol. 12, no. 1, pp. 316–327, Feb. 2024.

[3] Z. Shafiq and W. Egger, "Study of charging strategies of lithium batteries and their effect on the batteries technologies," in *Proc. IEEE 13th Annu. Inf. Technol., Electron. Mobile Commun. Conf.*, 2022, pp. 0540–0546.

[4] S. Lavety, R. K. Keshri, and M. A. Chaudhari, "Multistep constant current-constant voltage charging strategy for a valve regulated lead-acid battery," *IEEE Trans. Ind. Appl.*, vol. 57, no. 6, pp. 6494–6503, Nov./Dec. 2021.

[5] J. Deng et al., "Frequency and parameter combined tuning method of LCC–LCC compensated resonant converter with wide coupling variation for EV wireless charger," *IEEE J. Emerg. Sel. Topics Power Electron.*, vol. 10, no. 1, pp. 956–968, Feb. 2022.

[6] T. H. Abdelhamid, A. Elzawawi, and M. A. Elreazek, "Wireless power transfer analysis and power efficiency enhancement via adaptive impedance matching network," in *Proc. IEEE Int. Conf. Power Eng. Appl.*, 2021, pp. 91–96.

[7] Y. Li, J. Hu, F. Chen, Z. Li, Z. He, and R. Mai, "Dual-phase-shift control scheme with current-stress and efficiency optimization for wireless power transfer systems," *IEEE Trans. Circuits Syst. I, Regular Papers*, vol. 65, no. 9, pp. 3110–3121, Sep. 2018.

[8] Z. Yan et al., "Efficiency improvement of wireless power transfer based on multitransmitter system," *IEEE Trans. Power Electron.*, vol. 35, no. 9, pp. 9011–9023, Sep. 2020.

[9] H. Liu, J. Chen, H. Zhong, J. Liu, X. Wu, and G. Wei, "Analyze the wireless power transmission system with constant voltage output based on active impedance matching," in *Proc. 2nd Asia Power Elect. Technol. Conf.*, 2023, pp. 156–162.

[10] T.-D. Yeo, D. Kwon, S.-T. Khang, and J.-W. Yu, "Design of maximum efficiency tracking control scheme for closed-loop wireless power charging system employing series resonant tank," *IEEE Trans. Power Electron.*, vol. 32, no. 1, pp. 471–478, Jan. 2017.

[11] Z. Huang, S.-C. Wong, and C. K. Tse, "Control design for optimizing efficiency in inductive power transfer systems," *IEEE Trans. Power Electron.*, vol. 33, no. 5, pp. 4523–4534, May 2018.

[12] Y. Ma, K. Cui, Y. Sun, Z. Chen, and X. Fan, "A hybrid adaptive digital delay compensated active rectifier with PWM-based technique and resistor-array tuning for wireless power transmission," *IEEE Trans. Power Electron.*, vol. 37, no. 9, pp. 11423–11435, Sep. 2022.

[13] X. Xie, C. Xie, J. Wang, Y. Li, Y. Du, and L. Li, "Constant current output control based on cross-coupling compensation in multireceiver WPT system using active rectifier," *IEEE Trans. Transp. Electrific.*, vol. 9, no. 1, pp. 1960–1972, Mar. 2023.

[14] A. Desmoort, O. Deblecker, and Z. De Greve, "Active rectification for the optimal command of bidirectional resonant wireless power transfer robust to severe circuit parameters deviations," *IEEE Trans. Ind. Appl.*, vol. 56, no. 2, pp. 1640–1648, Mar./Apr. 2020.

[15] M. Wu et al., "A dual-sided control strategy based on mode switching for efficiency optimization in wireless power transfer system," *IEEE Trans. Power Electron.*, vol. 36, no. 8, pp. 8835–8848, Aug. 2021.

[16] S. Ann and B. K. Lee, "Analysis of impedance tuning control and synchronous switching technique for a semibridgeless active rectifier in inductive power transfer systems for electric vehicles," *IEEE Trans. Power Electron.*, vol. 36, no. 8, pp. 8786–8798, Aug. 2021.

[17] B. Zou and Z. Huang, "Primary-frequency-tuning and secondary-impedance-matching IPT converter with programmable constant power output and optimal efficiency tracking against variation of coupling coefficient," *IEEE Trans. Power Electron.*, vol. 39, no. 4, pp. 4895–4909, Apr. 2024.

[18] R. Mai, Y. Liu, Y. Li, P. Yue, G. Cao, and Z. He, "An active-rectifier-based maximum efficiency tracking method using an additional measurement coil for wireless power transfer," *IEEE Trans. Power Electron.*, vol. 33, no. 1, pp. 716–728, Jan. 2018.

[19] M. Li, J. Deng, D. Chen, W. Wang, Z. Wang, and Y. Li, "A control strategy for ZVS realization in LCC-S compensated WPT system with semi bridgeless active rectifier for wireless EV charging," in *Proc. IEEE Energy Convers. Congr. Expo.*, 2021, pp. 5823–5827.

[20] S. Lu, M. Böttigheimer, and N. Parspour, "An impedance mapping-based T-compensation network and control strategy for WPT system with full-bridge active rectifier," *IEEE Trans. Power Electron.*, vol. 38, no. 11, pp. 14675–14688, Nov. 2023.

[21] X. Zhang et al., "A control strategy for efficiency optimization and wide ZVS operation range in bidirectional inductive power transfer system," *IEEE Trans. Ind. Electron.*, vol. 66, no. 8, pp. 5958–5969, Aug. 2019.

[22] Y. Jiang, L. Wang, J. Fang, C. Zhao, K. Wang, and Y. Wang, "A joint control with variable ZVS angles for dynamic efficiency optimization in wireless power transfer system," *IEEE Trans. Power Electron.*, vol. 35, no. 10, pp. 11064–11081, Oct. 2020.

[23] J. Huang, X. He, P. Huo, and R. Xu, "A hybrid modulation strategy for LCC–LCC compensated bidirectional wireless power transfer system to achieve high efficiency in the whole operating range," *IEEE Trans. Ind. Electron.*, vol. 71, no. 1, pp. 327–337, Jan. 2024.

[24] S. Li, W. Li, J. Deng, T. D. Nguyen, and C. C. Mi, "A double-sided LCC compensation network and its tuning method for wireless power transfer," *IEEE Trans. Veh. Technol.*, vol. 64, no. 6, pp. 2261–2273, Jun. 2015.

[25] H. Li, L. Tan, R. Wang, and X. Huang, "Research and improvement of oscillation problems caused by active rectifier circuits in EV-WPT systems," *IEEE Trans. Power Electron.*, vol. 38, no. 10, pp. 13231–13242, Oct. 2023.

Haoze Li (Graduate Student Member, IEEE) was born in Jiangsu, China, in 1997. He received the B.S. degree in electrical engineering and automatic chemistry from Jiangsu University, Zhenjiang, China, in 2019. He is currently working toward the Ph.D. degree in electrical engineering with Southeast University, Nanjing, China.

His research interests include wireless power transfer, active rectifier, and high frequency power electronic conversion devices.

Linlin Tan (Member, IEEE) received the B.S. degree in electrical engineering and automation from Harbin Engineering University, Harbin, China, in 2008, and the Ph.D. degree in electrical engineering from Southeast University, Nanjing, China, in 2014.

He is currently an Associate Professor with the School of Electrical Engineering, Southeast University, Nanjing. He has authored or coauthored more than 30 papers and more than 40 inventions. His research interests include wireless power transfer, wireless charging for electric vehicles, and wireless V2G

Heqi Xu (Student Member, IEEE) was born in Jilin, China, in 1994. She received the M.S. degree in electrical engineering and automation from Qingdao University, Qingdao, China, in 2020. She is currently working toward the Ph.D. degree in electrical engineering with Southeast University, Nanjing, China.

Her research interests include wireless power transfer and magnetic coupler design.

Zhijun Wu (Graduate Student Member, IEEE) was born in Shijiazhuang, China, in 1994. He received the M.S. degree in biomedical engineering from Hebei University of Technology, Tianjin, China, in 2021. He is currently working toward the Ph.D. degree in electrical engineering with Southeast University, Nanjing, China.

His research interests include wireless power transfer and simultaneous wireless power and data transfer.

Xueliang Huang (Member, IEEE) was born in Zhoushan, China, in 1969. He received the B.S., M.S., and Ph.D. degrees in electrical engineering from Southeast University, Nanjing, China, in 1991, 1994, and 1997, respectively.

From 2002 to 2004, he was a Postdoctoral Researcher with the University of Tokyo. Since 2004, he has been a Professor with the Department of Electrical Engineering, Southeast University. He has authored four books, more than 150 articles, and more than 40 inventions. He holds one PCT patent. His research interests include novel wireless power transfer systems, analysis of electromagnetic field, applied electromagnetics, and intelligent electricity technology.

Prof. Huang is an Editor for the *Journal Transactions of China Electrotechnical Society*.